Charge Transport through Electrospun SnO 2 Nanoflowers and Nanofibers: Role of Surface Trap Density on Electron Transport Dynamics

5 AUTHORS, INCLUDING:

Rajan Jose
Universiti Malaysia Pahang
152 PUBLICATIONS **3,231** CITATIONS

SEE PROFILE

Archana Panikar
University of Alabama
5 PUBLICATIONS **93** CITATIONS

SEE PROFILE

Chellappan Vijila
Agency for Science, Technology and Research …
69 PUBLICATIONS **627** CITATIONS

SEE PROFILE

Seeram Ramakrishna
National University of Singapore
407 PUBLICATIONS **14,471** CITATIONS

SEE PROFILE

Charge Transport through Electrospun SnO₂ Nanoflowers and Nanofibers: Role of Surface Trap Density on Electron Transport Dynamics

Naveen Kumar Elumalai,[†] Rajan Jose,*[‡] Panikar Sathyaseelan Archana,[†] Vijila Chellappan,[§] and Seeram Ramakrishna*[†,§]

[†]National University of Singapore, Singapore 117576

[‡]Universiti Malaysia Pahang, 26300 Pahang, Malaysia

[§]Institute of Materials Research and Engineering (IMRE), Agency for Science, Technology and Research (A*STAR), 3 Research Link, Singapore 117602

Ⓢ Supporting Information

ABSTRACT: A larger amount of tin precursor was dispersed in electrospun polyvinyl acetate fibers than that required for SnO₂ fiber formation upon annealing, thereby creating a constraint such that all nuclei formed during annealing could not be accommodated within the fiber, which leads to enhanced reaction kinetics and formation of highly crystalline–cum–higher surface area SnO₂ flowers. The flowers are shown to have a lower density of surface trap states than fibers by combining absorption spectra and open circuit voltage decay (OCVD) measurements. Charge transport through the SnO₂ flowers in the presence of the iodide/triiodide electrolyte was studied by OCVD, electrochemical impedance spectroscopy, and transient photodecay techniques. The study shows that the flowers are characterized by higher chemical capacitance, higher recombination resistance, and lower transport resistance compared with fibers. Photocurrent transients were used to extract the effective electron diffusion coefficient and mobility which were an order of magnitude higher for the flowers than that for the fibers. The flowers are also shown to have an enhanced Fermi energy, on account of which as well as higher electron mobility, dye-sensitized solar cells fabricated using the SnO₂ flowers gave V_{OC} ~700 mV and one of the highest photoelectric conversion efficiencies achieved using pure SnO₂.
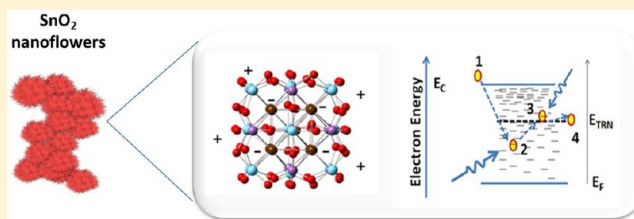
1. INTRODUCTION

Functional nanostructured metal oxide semiconductors (n-MOS) possessing simultaneously a large specific surface area and a high electron mobility have been actively sought in recent years to fabricate high performance nanoelectronic devices such as dye-sensitized solar cells (DSCs).[1−4] An inverse relationship exists between the above two properties; i.e., the electron mobility is inversely proportional to the specific surface area of n-MOS. High surface-to-volume ratio of nanomaterials results in relaxation of equilibrium bond lengths and angles in the atomic arrangement of nanomaterials compared with their bulk counterparts.[5] This deviation gives rise to a broad distribution of localized energy states that lie within the band gap;[5−7] i.e., unlike that of bulk semiconductors, the band gaps of n-MOS are not completely forbidden (Figure 1). In the case of bulk semiconductors, the electrons move via direct hopping from one transport state to another through its conduction band. On the other hand, in the case of n-MOS, they are trapped at the interband gap-lying energy states and subsequent thermal activation leads them to deeper energy levels and retrap again (Figure 1).[6,8] Thus, the electrons undergo multiple trappings and eventually move through a transport level (E_{TR}) that lies in the band gap (Figure 1).[6,8] In addition, bulk materials could

support an electric field on account of a space charge region which would further accelerate the electrons, whereas the space charge is completely depleted in the case of nanomaterials (≤25 nm) and could not support a macroscopic electric field.[9] The electron mobility through the multiple trapping mode is therefore several orders of magnitude lower than that through the direct hopping mode, thereby imposing detrimental effects on the device performance.[10] The electron energy loss and subsequent thermalization of photoinduced carriers during transport in DSCs are, therefore, a subject of intense discussion recently.[11−14]

Tin oxide (SnO₂), an archetypical transparent conducting oxide with larger band gap (~3.6 eV at 300 K) and higher electrical conductivity than other metal oxide semiconductors, is a candidate for a number of applications as transparent conducting electrodes,[15−18] electrodes for solar cells,[19−21] batteries,[22,23] gas sensors,[24,25] and other optoelectronic devices.[26,27] Considerable efforts have been devoted to develop its nanostructures with diverse morphologies and aspect ratios
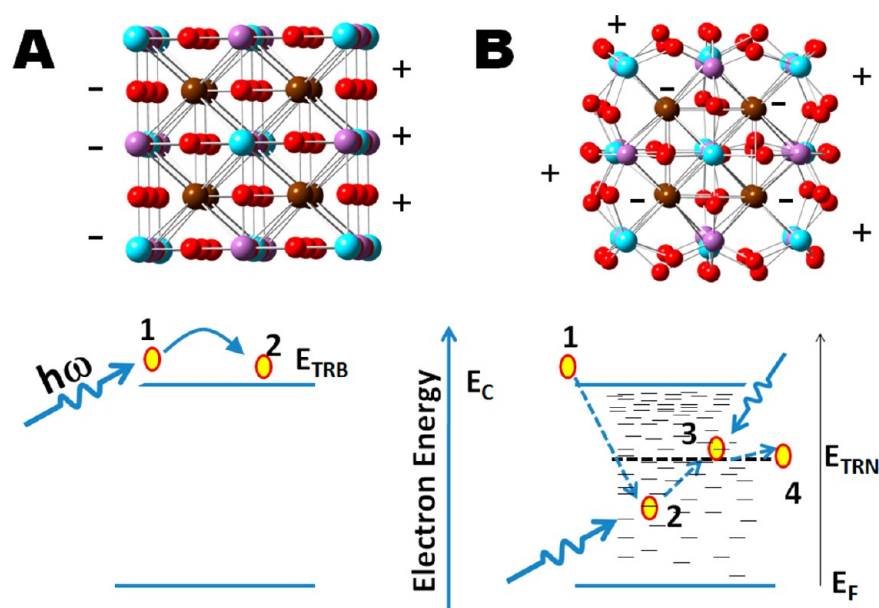
Figure 1. Schematics showing the difference in the charge diffusion mechanism between (A) bulk single crystalline semiconductors and (B) nanocrystalline semiconductors. The top panels show the difference in periodic arrangements of atoms between single crystalline and nanocrystalline materials ,and the bottom panels are the difference in their band structures. E_C and E_F denote the conduction band minimum and Fermi energies, respectively. The circles represent electrons. The solid arrow in (A) denotes the hopping of electrons through the bulk transport state (E_{TRB}); the dashed line in (B) indicates the transport through the band gap states (E_{TRN}). The counting numbers indicate the arbitrary electronic positions after each hopping. The atoms in bulk solids are at their equilibrium positions; therefore, the unsaturated charges (shown by + and − signs) are only at the surface, thereby creating an internal electric field. This electric field further accelerates the electrons in bulk crystals. On the other hand, the "off-centering" of the atoms in the nanomaterials redistributes the charges such that the electric field is removed.

with an aim to enhance the specific surface area and further improve their properties such that a given function can be served with a minimal amount of materials.[28−30] Nonconventional morphologies of SnO_2 such as tetrapodes and flowers are also synthesized from colloidal solutions with improved and/or modified properties compared to their particulate or one-dimensional analogues.[11,31]

Owing to the ability of the electrospinning technique to produce nanomaterials on a commercial scale,[32−34] compared with most of the colloidal wet-chemical methods, we have synthesized flowers of SnO_2 by controlling the precursor concentration in electrospun polyvinyl acetate (PVAc) fibers.[35] A larger amount of tin precursor was dispersed in PVAc fibers than that required for SnO_2 fiber formation upon annealing, thereby creating a constraint such that all nucleii formed during annealing could not be accommodated in it. This constraint lead to enhanced reaction kinetics and formation of highly crystalline−cum−higher surface area SnO_2 flowers (see the Supporting Information).[35] The DSCs fabricated using the SnO_2 flowers showed record open circuit voltage (V_{OC}) and gave one of the highest photoconversion efficiencies ever achieved using pure SnO_2 as a photoelectrode. The purpose of the present paper is to determine the difference in their electronic band properties, especially electron density of states, positions of their Fermi level, as well as electron diffusivity (D_n) and mobility (μ_n). Our results demonstrate that the flowers are characterized by a lesser density of surface traps while maintaining a larger surface area than the fibers and have higher electron density of states, enhanced recombination resistance, and lower transport resistance.

2. EXPERIMENTAL PROCEDURES

The SnO_2 flowers were synthesized by the electrospinning technique as described before.[35] Briefly, a 6 mM solution of $SnCl_2$ was produced by dissolving it in a mixture of PVAc, dimethylformamide, and ethanol. The solution was electrospun at ~25 kV with an injection rate of ~1 mL/h to fabricate polymeric fibers containing the Sn precursor. The fibers upon heating at 500 °C yielded SnO_2 flowers. Similarly, SnO_2 nanofibers were also produced by electrospinning using a 3 mM precursor solution. The SnO_2 flowers and fibers were characterized by BET surface area measurements (NOVA 4200E surface area and pore size analyzer, Quantachrome, USA), powder X-ray diffraction (XRD, Bruker-AXS D8 ADVANCE Powder X-ray diffractometer), field emission scanning electron microscopy (FE-SEM, Quanta 200 FEG System, FEI Company, USA, operated at 20 kV), and high resolution transmission electron microscopy (HR-TEM, JEOL 3010 operated at 300 kV). The optical band gap of the materials was determined from the absorption spectral measurements (UV−visible-NIR Spectrophotometer, UV-3600, Shimadzu). The materials were ultrasonically dispersed in methanol, and a transparent coating was made on a glass slide for absorption spectral measurements.

The polymeric fibers containing the precursors for formation of flowers and fibers were developed onto separate FTO glass substrates (1.5 cm × 1 cm; 25 $\Omega/\square$, Asahi Glass Co. Ltd., Japan) to fabricate DSCs. The films were annealed at 80 °C in an oven and then wrapped in aluminum foil which subsequently hot-pressed (Stahls' Hotronix 6 × 6 press, USA) at ~200 °C with a pressure of 0.4 MPa for 15 min to homogenize the surface and improve adhesion with the FTO substrate. The hot-pressed films were then annealed at 500 °C for 30 min. The thickness of the films and its surface uniformity

were studied by surface profilometry (Alpha−Step IQ Surface Profiler). The films were homogeneous; therefore, a difference in properties does not arise from the surface nonuniformity. The DSCs were prepared by soaking a 0.28 cm^2 SnO$_2$ electrode of ∼15 μm thickness in a dye solution containing a 1:1 volume mixture of acetonitrile and *tert*-butanol of a ruthenium-based dye [RuL$_2$(NCS)$_2$-2H$_2$O; L = 2,2′-bipyridyl-4,4′-dicarboxylic acid (0.5 mM), N3 Solaronix)] for 24 h at room temperature. The dye-sensitized samples were then washed in ethanol to remove unanchored dye and dried in air. The dye-anchored electrodes were sealed using a 50 μm spacer. Acetonitrile containing 0.1 M lithium iodide, 0.03 M iodine, 0.5 M 4-*tert*-butylpyridine, and 0.6 M 1-propyl-2,3-dimethyl imidazolium iodide was used as the electrolyte. A Pt sputtered FTO glass was used as the counter electrode. Photocurrent measurements were carried out by a XES-151 S solar simulator (San Ei, Japan) under AM1.5G conditions. The level of standard irradiance (100 mW/cm^2) was set with a calibrated c-Si reference solar cell. Data acquisition was facilitated by an Autolab PGSTAT30 (Eco Chemie B.V., The Netherlands) integrated with a potentiostat. The open circuit voltage decay (OCVD) of the two devices was obtained by closing the illumination source and recording the fall of V_{OC} using the Autolab instrument (PGSTAT30). The AC responses of the cells were studied by electrochemical impedance spectroscopy (EIS) using the Autolab PGSTAT30. The EIS measurements were carried out in the dark using 10 mV ac voltage superimposed on a forward-biased DSC (0.4−0.7 V) with frequency ranging from 30 kHz to 0.05 Hz.

Electron diffusivity (D_n) and mobility (μ_n) through the DSCs were studied by transient photocurrent measurements. The DSCs were excited with a low intensity laser pulse (532 nm Nd:YAG laser, pulse width <5 ns) superimposed on a large background white light illumination. The intensity of the white bias light was varied to study the effect of photocarrier density on D_n. The intensity of the laser light was controlled with neutral density filters to keep the magnitude of photocurrent transients less than the dc level due to the white bias light. The cells were illuminated through the substrate as well as the counter electrode sides. The photocurrent transients were recorded using a digital oscilloscope (Agilent, 1 GHz) under short circuit conditions. The RC time constant of the instrument was <20 μs.

3. RESULTS AND DISCUSSION

3.1. Structural and Morphological Characteristics of Flowers and Fibers.

Detailed structural and morphological characteristics of the electrospun SnO$_2$ flowers and fibers are published in our previous publication.[35] Briefly, Figure 2 shows a difference in morphologies of the electrospun flowers and fibers produced as a result of a difference in the Sn precursor concentration. The fibers consisted of grains of ∼50 nm and had a diameter of ∼200 nm, whereas the flowers had an overall diameter of ∼400 nm and were made up of rods of length ∼80 nm. The flowers had enhanced crystallinity, which is judged from the extended periodicity of the high-resolution TEM images and sharpness of the selected area diffraction patterns, than the fibers (see the Supporting Information). The XRD patterns of the flowers and fibers were similar, indicating that the two morphologies are chemically identical (see the Supporting Information).[35] The BET specific surface area of the flowers was double (40 m^2/g) that of the fibers (19 m^2/g). Simultaneous high specific surface area and high crystallinity are
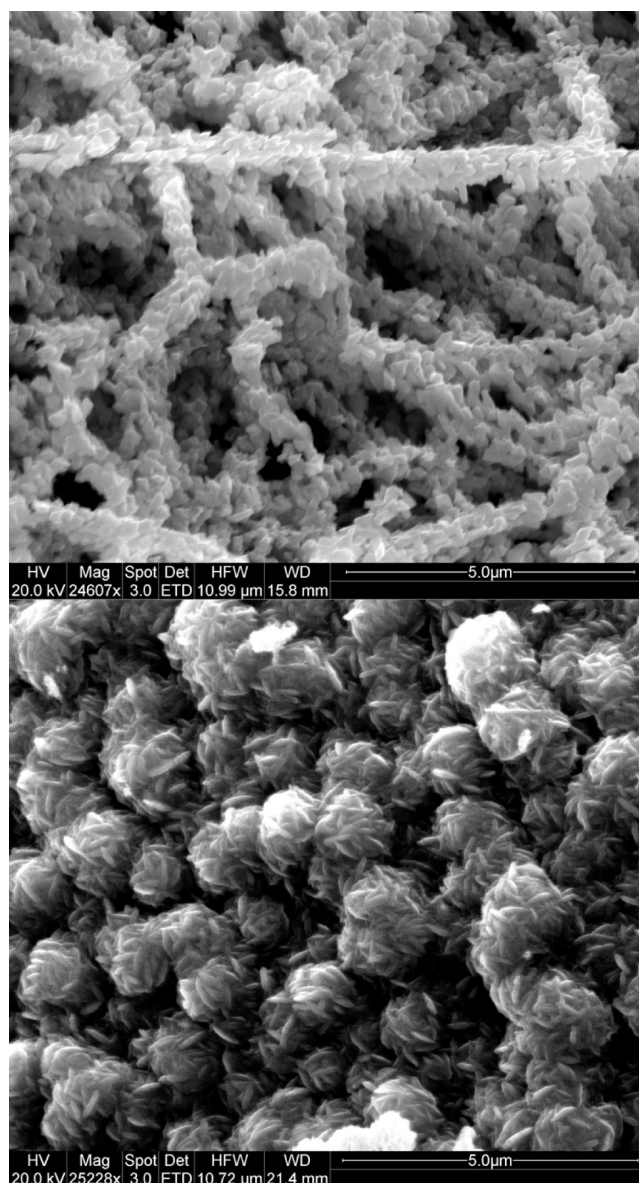

Figure 2. FESEM image of the fibers (top) and flowers (bottom).

rather rare in the same material, which in the present case originated from the reaction kinetics when the crystallites are constrained to grow within a smaller volume.

3.2. Photovoltaic Parameters of the Flower and Fiber Based DSCs.

Figure 3 shows current density (J_{SC}) vs voltage (V) plots of the DSCs fabricated using the SnO$_2$ flowers and fibers. The flower-based DSC showed V_{OC} ∼700 mV, J_{SC} ∼7.30 mA/cm^2, fill factor (FF) ∼59.6%, and η ∼3.0%, which for the fiber based device was V_{OC} ∼600 mV, J_{SC} ∼3.0 mA/cm^2, FF ∼38.3, and η ∼0.71%, respectively; i.e., the flower based device shows ∼140% increased J_{SC}, ∼16% increased V_{OC}, and ∼55% increased FF compared with the fiber based device. The V_{OC} values obtained using the flowers are the highest observed using pure SnO$_2$; however, similar or higher V_{OC} values were previously obtained with surface modifications.[19,31] Two possible reasons for the enhanced performance of the flower based devices are (i) higher dye-loading on account of its higher specific surface area than the fibers and (ii) its improved charge transport characteristics compared with the fiber based devices. The dye-loading, which was normalized with respect to
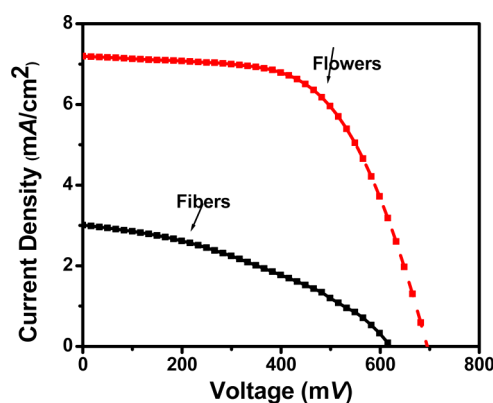
Figure 3. I−V characteristics of the DSCs fabricated using flowers and fibers.

Figure 4. Absorption spectra of flowers and fibers showing band edge and band tail energy states.

the electrode geometric area measured from the desorption test, was 2.12×10^{-7} and 1.84×10^{-7} mol/cm^2 for flower and fiber based devices, respectively (see the Supporting Information). The differences in dye-loading result from the differences in specific surface areas of the flowers and fibers with which the electrodes were fabricated. The J_{SC} normalized with respect to the dye-loading for the flowers (3.44 mA/mol) was more than twice that for the fibers (1.63 mA/mol), thereby indicating that the flowers have enhanced charge transport kinetics also.

3.3. Difference in Electronic Bands of SnO₂ Flowers and Fibers. Prior to discussing the charge transport kinetics through the flowers and fibers, it is imperative to discuss their electronic band properties. As described in the Introduction section, random deviation of equilibrium bond lengths and angles in the lattice of nanocrystalline materials compared to their bulk counterpart introduces potential fluctuations that allow energy levels, known as band tail states (synonomously, "surface atomic states", "surface traps") within the forbidden energy gap (Figure 1). The occurrence of a band tail in nanocrystalline, amorphous, and disordered materials is revealed in their absorption spectra as a broad exponentially decreasing profile, known as the Urbach tail, along the energy scale below the band edge absorbance.[36−38] This distribution has the expression[6]

$$g_L(E) = \frac{N_L}{k_B T_o} \exp[(E - E_o)/k_B T_o] \qquad (1)$$

where k_B is the Boltzmann constant, N_L is the total density of states, E_o is the bottom of the conduction band energy, and T_o is a parameter having temperature units that determines the depth of the distribution of the localized states.

Figure 4 is the Tauc plot developed from the experimental absorption spectra of the flowers and fibers recorded under identical conditions. The optical band gaps of the two morphologies were calculated from the experimental absorption spectrum using the Tauc equation

$$\alpha v = C \left[\frac{h v - E_g}{h v} \right] \qquad (2)$$

where C is a constant, $h v$ is the photon energy, and E_g is the band gap energy. The value of E_g was determined from absorption onset of $[(\alpha h v)^2$ vs $h v]$ curves. Similar absorption onset was observed for both structures, giving a band gap energy of ∼3.6 eV, consistent with other reports.[39] Note that
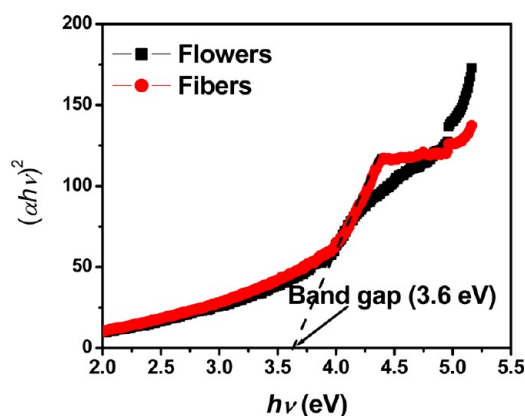
the Mott−Schottky analysis also gave similar flat band potentials for the two types of structures.[35] The spectra showed an exponentially decreasing profile that red-shifted to the band edge absorption, indicating the existence of band tail states on account of their nanocrystallinity. From the similarity in the absorption spectra, one could observe similar E_o and T_o for both structures. No attempt was made to quantify the above parameters as well as trap density from the band tails of the absorption spectra in this report because of the fact that the observed spectra could be a convolution of several scattering parameters arising from opacity and surface irregularities.

The OCVD, which measures the temporal decay of V_{OC} upon removing the illumination source in a dye-sensitized solar cell operating at steady state, provides an electrical method of mapping the distribution of band tail states.[40] Under steady state in DSCs, the electrons injected into the photoelectrode are equal to that removed from the contact electrode. When the electron injection is terminated by closing the light source, the electrons in the conduction band of SnO₂ decay faster through the contact electrode, whereas the ones at the trap states will be delayed depending on their lifetime. Consequently, the V_{OC} shows a delay before reaching zero, which is typically measured in the OCVD. As the measurement is performed in the dark, recombination with the oxidized dye-molecule does not take place, but this is acceptable because the electrolyte accounts for the majority of the recombination even under illumination.[41] Assuming a first order recombination reaction, the electron lifetime (τ_n) as a function of voltage is given by $\tau_n = -(kT/e)(dV_{OC}/dt)^{-1}$,[42,43] where kT is the thermal energy, e is the positive elementary charge, and dV_{oc}/dt is the first order time derivative of the V_{OC}. Figure 5 compares the τ_n of the flowers and fibers as a function of voltage determined from the OCVD curves (see the Supporting Information), which clearly shows that the decay profile and hence the density of band tail states of both structures vary considerably. The fibers showed an enhanced τ_n for higher V_{OC}'s, most probably because of the more channeled charge transport through them compared with that of the flowers. The τ_n of both morphologies showed exponential dependences in the 0.5−0.7 V range, showing the diffusion through bulk traps. Following the exponential dependence, a lowering of τ_n was observed in the 0.2−0.4 V range of both structures, the magnitude of which was small for the flowers but appreciable for the fibers. This lowering occurs as a result of the electrons falling in surface deep-traps; i.e., the flowers have a lower trap density compared to fibers, the source
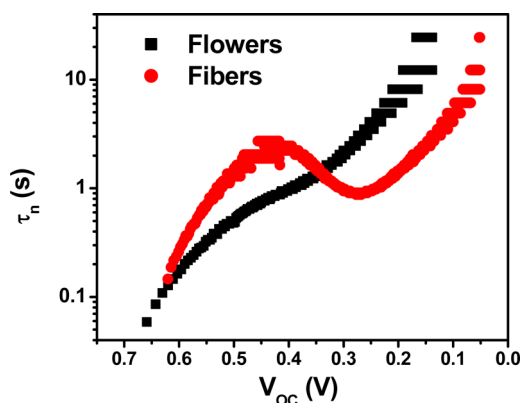
Figure 5. The calculated lifetime from the OCVD curves. The experimental OCVD curves are in the Supporting Information.

3.4. Charge Transport through the SnO$_2$ Nanoflowers and Nanofibers.

Electrochemical impedance spectroscopy (EIS) has emerged as a powerful tool to study the charge transport kinetics at the electrode in DSCs. The EIS curves of the flower- and fiber-based devices are presented in the Supporting Information. The EIS data of DSCs is usually compared with an electrical equivalent comprised of resistors and capacitors (Figure 6), which represents various interfacial and transport processes in DSCs, to extract the parameters corresponding to the diffusion and recombination processes.[46,47] The EIS spectra of DSCs typically display three semicircles on account of three processes (see the Supporting Information); viz., (i) charge transport resistance occurs at high frequency (>1 kHz), (ii) charge transfer resistance occurs at intermediate frequencies (1 kHz < f < 1 Hz), and (iii) ion diffusion occurs at lower frequencies (<1 Hz).

The grains composing the flowers and the fibers are of sufficiently larger size (50−80 nm) to support a space charge region; therefore, they could exhibit frequency dependent interfacial capacitance. Therefore, the capacitors in the electrical equivalent are replaced by a constant phase element (CPE).[48] The charge transport parameters can be calculated from the transmission line as follows. For a device of electrode thickness L, the electron transport resistance in the electrode material is $R_T = r_t L$. The interfacial charge recombination resistance $R_{CT} = r_{ct}/L$ and the chemical capacitance $C_\mu = c_\mu/L$ are indicative of recombination with the electrolyte and electron density of the electrode material, respectively.[49] τ_n was calculated from $\tau_n = (r_{ct}c_\mu)^{1/\beta}$, where β is the CPE exponent. r_t, c_μ, r_{ct}, and β are components of the transmission line as defined in ref 46.

Figure 7 shows the characteristic data corresponding to the electron density of states and recombination extracted from the EIS data using the recombination model described above for

of which is expected to be the enhanced crystallinity. Similar lowering of τ_n and enhanced trap density are reported in materials of lower crystallinity including most frequently used TiO$_2$ in DSCs.[44,45] More interestingly, a reversal in τ_n was observed at lower V_{OC}'s, i.e., after the deep-trap, thereby further confirming that the fibers are characterized by a higher density of surface traps.

Thus, it could be concluded from the absorption spectra and the OCVD studies that (i) band tail states consisting of localized energy states arise due to the deviation from ideal atomic packing exist in SnO$_2$ flowers and fibers, (ii) the depth of the distribution and bottom of the conduction band energy appears to be similar for both structures, (iii) however, fibers have an enhanced trap density on account of their lower crystallinity.
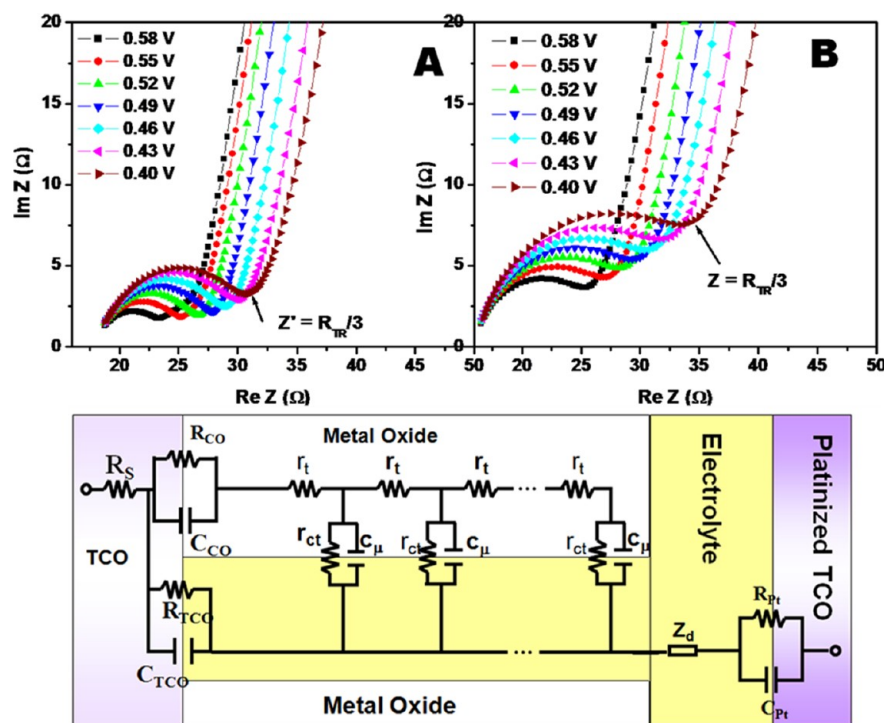

Figure 6. Difference in EIS curves in the high frequency region of the flowers and fibers (top); the electrical equivalent of a dye-sensitized solar cell used in this work to elucidate charge transport parameters (bottom).
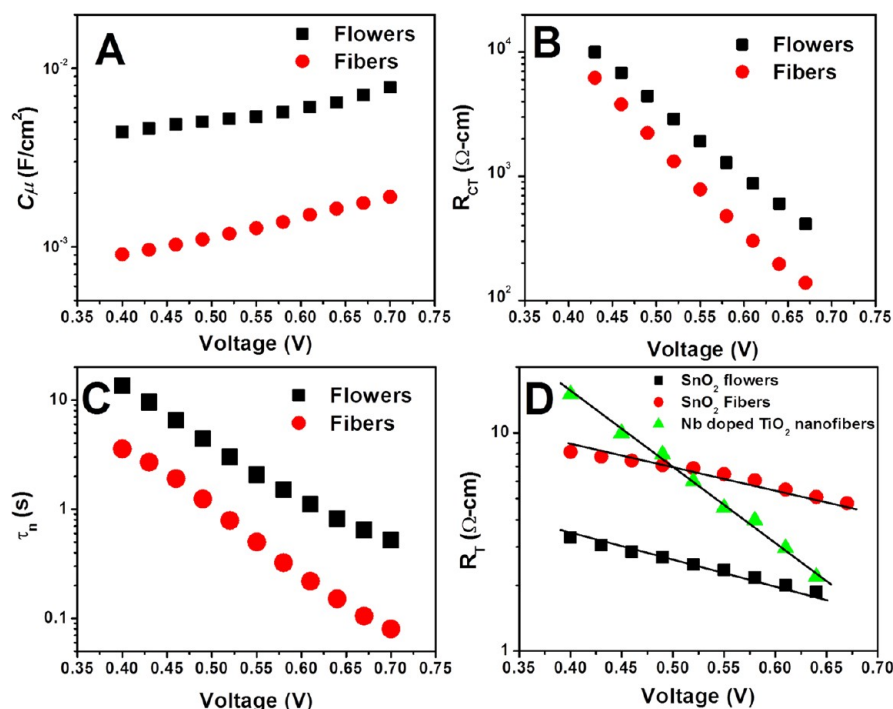
Figure 7. Transport parameters of the flowers and fibers. (A) Chemical capacitances, which is a measure of the chemical capacitance, as a function of applied voltage; (B) electron recombination resistances; (C) electron lifetime; and (D) charge transport resistance. The charge transport resistance of similar transparent conducting oxide, i.e., niobium doped TiO_2 nanofibers, is also shown for comparison.

the two types of devices. Figure 7A is the difference in C_μ normalized with respect to the electrode area for the flowers and the fibers. Both curves showed an exponential dependence on applied voltage as normally expected.[50] Obviously, the flowers are characterized by at least an order of magnitude higher C_μ compared with that of the fibers.

C_μ has a contribution from the total density of electronic states in the conduction band (N_C) as well as in the band tail (N_L) states.[8,50] If we assume similar N_C for both structures by considering the fact that the particles composing them are much higher than the exciton Bohr radius of SnO_2 (~2.7 nm), the difference in the C_μ results from the density of band tail states. For a given Fermi level, C_μ has the form

$$C_\mu = \frac{N_L e^2}{k_B T_o} \exp[(E_F - E_0)/k_B T_o] \qquad (3)$$

As discussed in section 3.3, E_0 and T_0 can be considered similar for the two materials. Therefore, it follows that, even with a lower N_L, if the flowers show enhanced C_μ, it certainly indicates that E_F of flowers are at higher energies than that of the fibers. Therefore, as $V_{OC} \alpha (F_{n1} - F_{n2})$, where F_{n1} is the Fermi energy of the photoelectrode and F_{n2} is the electrochemical potential energy of the electrolyte, the flower based device shows an increased V_{OC}. Considering the physicochemical characteristics of these two morphologies, the enhanced E_F of the flowers can only be attributed to its enhanced crystallinity and lowered trap-density. Lowering of density in weakly crystalline materials is because of the fact that the atomic deviations in them result in delocalization of electrons. Consequently, a well ordered crystal lattice offers close lying orbitals, leading to enhanced E_F. Therefore, enhancement in E_F is not surprising for materials with higher crystallinity; however, in this case, it is accompanied by a 2-fold increase in the specific surface area which is rather rare.

R_{CT} showed an exponential decay with applied voltage for the two types of morphologies (Figure 7B). R_{CT} (flowers) > R_{CT} (fibers). Electron recombination with the hole-conductor in DSCs mainly depends on the (i) energy of the conduction band edge and (ii) τ_n. As the band edges and band gaps are similar for the two types of morphologies, the recombination rate constant as a result of case (i) does not differ. Therefore, the difference in R_{CT} in the two types of morphologies arises from different τ_n. The τ_n extracted from the EIS curves, shown in Figure 7C, exhibited an exponential dependence with voltage and also higher values for the flower structure. Flowers showed enhanced τ_n at all voltages unlike that observed in OCVD studies (Figure 5). Remember that the OCVD showed that, for fiber based devices, τ_n was higher at higher voltages and lower at lower voltages. This variation could arise from the difference in time domain involved in both measurements—the OCVD measures the real time electron decay in the absence of an applied electric field, whereas the EIS measurements employ a bias voltage. The electrons diffuse because of the electron concentration gradient with a D_n in the absence of an electric field, whereas they are accelerated by it otherwise. Therefore, the τ_n and corresponding properties that include a temporal component such as D_n and μ_n calculated from EIS measurements are expected to be an overestimation. Nevertheless, both measurements show that flowers are characterized by a higher τ_n over an appreciable range of voltage and, therefore, could be a better choice to build more highly efficient DSCs than the fibers.

Figure 7D shows R_T as a function of applied voltage extracted from the EIS analysis using the transmission line model. Ideally, higher R_{CT} and lower R_T are preferred for a high performance device. Interestingly, the flowers are characterized by lower R_T and higher R_{CT} compared with that of the fibers despite the fact that one-dimensional nanostructures, both in the ordered and

disordered geometries, such as nanowires, rods, and fibers, are shown to have lower transport resistance on account of guided transport. However, the crystallinity of the two morphologies is remarkably different and, as shown in section 3.3, the band gap of fibers has a high density of localized energy states. Therefore, the lower R_T of the flowers could only be attributed to its high crystallinity, as a more ordered lattice contributes to less resistivity. Dou et al. recently showed similar R_T for highly crystalline Zn doped SnO_2 flowers.[31] However, in general, it is unlikely that flower morphology is more favorable for enhanced charge transport properties than the one-dimensional morphologies; rather, it is a function of crystallinity and guided transport. Note that removal of band tail states in nanofibers has also been shown to promote the charge transport considerably.[51] Figure 7D shows that the SnO_2 nanostructures show a weak dependence of R_T on applied voltage, thereby indicating more metallic conduction through them compared with a similar transparent conducting oxide, viz., the niobium doped TiO_2.

Furthermore, the D_n and μ_n through the flowers and fibers in the presence of the iodide/triiodide electrolyte were determined from transient photocurrent measurements. Figure 8 shows typical photocurrent transients observed for the
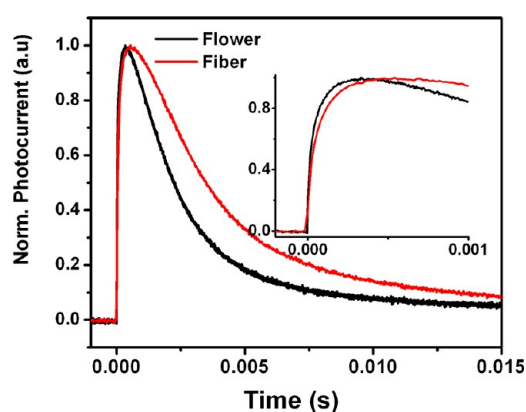

Figure 8. Charge decay behavior of the flower and fiber based devices. The inset shows the difference in photocurrent rise times.

flowers and fibers. The photocurrent was observed immediately after laser excitation in the device and reaches the peak at around 90 μs followed by an exponential decay. The photocurrent rise time of the flower based device was faster compared with the other. The decay time (τ_c) was extracted by fitting the photocurrent transient using a single exponential decay. The decay times normalized with respect to the thickness of the cells as well as μ_n calculated from D_n, which will be described below, using Einstien's relation are in Table 1. Table 1 also compares the decay times of SnO_2 nanowires and nanoparticles,[19] electrospun TiO_2 nanowires,[51] and niobium doped TiO_2[52]—another transparent conducting oxide of considerable interest. The flower-like morphology displayed the lower decay time, implying faster charge transport through them in agreement with the results of OCVD and EIS.

The D_n of electrons through the flower and fiber structure was estimated using the relation $\tau_c = d^2/2.35D_n$, where d is the thickness of the samples. The factor 2.35 corresponds to the diffusion geometry.[53,54] The electron collection time or transport time reported in this study is estimated from the long time domain of the transient photocurrent signal, which is

Table 1. Comparison of Nomalized Transition Time and Electron Mobility of the SnO_2 with Popular Metal Oxide Semiconductors

morphology	transit time (ms)	electron mobility $(cm^2\ V^{-1}\ s^{-1})$ $\times 10^{-3}$
SnO_2 fibers	10	3.75
SnO_2 flowers	2	18.5
SnO_2 nanowires[20]	2.7	13.7
SnO_2 nanoparticles[20]	10.2	3.63
Nb doped TiO_2 nanowires[52]	0.2	18.5
electrospun TiO_2 nanowires[51]	5.5	6.74
TiO_2 nanoparticles[12]	15	2.47

independent of the absorption coefficient or the illumination direction of the probe light. Figure 9 shows the D_n through the
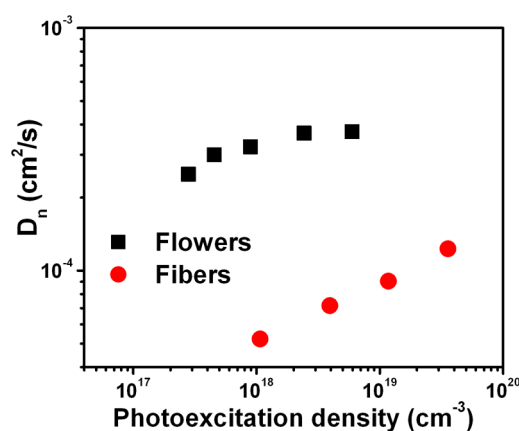

Figure 9. Electron diffusion coefficients of the flower and fiber based devices.

flower- and fiber-based devices, which was an order of magnitude higher for flowers than that for the fibers. At a photoexcitation density of $\sim 6 \times 10^{18}/cm^3$, the flowers gave a D_n of $\sim 3.74 \times 10^{-4}$ cm^2/s, which for the fibers was $\sim 7.572 \times 10^{-5}$ cm^2/s. This value is nearly 4 orders of magnitude higher than that reported using TiO_2 nanoparticles and 2.5 times higher than electrospun TiO_2 nanowires.[51] The D_n values of the flowers were independent of photoexcitation density, showing the diffusion through band edges which happens for materials with enhanced electron density and Fermi energy.[12,55] On the other hand, D_n showed a dependence on photoexcitation density, indicating a high density of surface traps on account of their inferior crystallinity.[56]

4. CONCLUSIONS

In conclusion, we have undertaken studies on the difference in band structure and charge transport properties of SnO_2 flowers and fibers developed by the electrospinning technique from polymeric solutions differing in tin precursor concentration. The absorption spectra of the flowers and the fibers show that they have similar band gaps; however, the open circuit voltage decay measurements show that flowers are characterized by a lower density of surface traps in the band gap on account of their enhanced crystallinity. It is shown that the SnO_2 flowers have a higher Fermi energy than that of the fibers owing to which a record open circuit voltage was obtained when the flowers were used as an anode in the dye-sensitized solar cells.

The flowers are also characterized by higher chemical capacitance, higher electron recombination resistance, and lower charge transport resistance which are beneficial in getting a higher short circuit current density in flower-based dye-sensitized solar cells. The superior charge transport properties of the flowers are attributed to their enhanced crystallinity. Very importantly, enhanced crystallinity in the SnO_2 flowers coexisted with a 2-fold BET specific surface area compared with the fibers, the simultaneous occurrence of which is rather rare. The transient photocurrent measurements were employed to extract the effective electron diffusivity and mobility of both SnO_2 morphologies. The SnO_2 flowers gave an order of magnitude higher electron diffusivity and mobility compared with the conventional SnO_2 and TiO_2 morphologies and, therefore, could be an acceptable material for nanotechnology applications requiring high surface area and electron mobility.

■ ASSOCIATED CONTENT

Ⓢ Supporting Information

The schematics showing the difference in morphology result due to the variation of precursor concentration, bright field TEM images, high resolution lattice images, selected area diffraction patterns of flowers and fibers, absorption of spectra showing the dye-loading results, open circuit voltage decay as a function of time, and XRD of both the nanostructures. This material is available free of charge via the Internet at http://pubs.acs.org.

■ AUTHOR INFORMATION

Corresponding Author
*E-mail: rjose@ump.edu.my (R.J.); seeram@nus.edu.sg (S.R.).

Notes

The authors declare no competing financial interest.

■ REFERENCES

(1) Bisquert, J. *ChemPhysChem* **2011**, *12*, 1633−1636.
(2) Jose, R.; Thavasi, V.; Ramakrishna, S. *J. Am. Ceram. Soc.* **2009**, *92*, 289−301.
(3) Hagfeldt, A.; Boschloo, G.; Sun, L.; Kloo, L.; Pettersson, H. *Chem. Rev.* **2010**, *110*, 6595−6663.
(4) Grätzel, M. *Acc. Chem. Res.* **2009**, *42*, 1788−1798.
(5) Jose, R.; Zhanpeisov, N. U.; Fukumura, H.; Baba, Y.; Ishikawa, M. *J. Am. Chem. Soc.* **2006**, *128*, 629−636.
(6) Bisquert, J. *J. Phys. Chem. C* **2007**, *111*, 17163−17168.
(7) Monroe, D. *Phys. Rev. Lett.* **1985**, *54*, 146−149.
(8) Bisquert, J. *Phys. Chem. Chem. Phys.* **2008**, *10*, 49−72.
(9) Grätzel, M. *Inorg. Chem.* **2005**, *44*, 6841−6851.
(10) Bisquert, J.; Fabregat-Santiago, F.; Mora-Seró, I.; Garcia-Belmonte, G.; Giménez, S. *J. Phys. Chem. C* **2009**, *113*, 17278−17290.
(11) Tétreault, N.; Arsenault, E.; Heiniger, L. P.; Soheilnia, N.; Brillet, J.; Moehl, T.; Zakeeruddin, S. M.; Ozin, G. A.; Grätzel, M. *Nano Lett.* **2011**, *11*, 4579−4584.
(12) Kopidakis, N.; Benkstein, K. D.; van de Lagemaat, J.; Frank, A. J.; Yuan, Q.; Schiff, E. A. *Phys. Rev. B* **2006**, *73*, 045326.
(13) Barnes, P. R. F.; Liu, L.; Li, X.; Anderson, A. Y.; Kisserwan, H.; Ghaddar, T. H.; Durrant, J. R.; O'Regan, B. C. *Nano Lett.* **2009**, *9*, 3532−3538.
(14) Snaith, H.; J.;Humphry-Baker, R.; Chen, P.; Cesar, I.; Zakeeruddin, S. M.; Grätzel, M. *Nanotechnology* **2008**, *19*, 424003.
(15) Sun, C.; Mathews, N.; Zheng, M.; Sow, C. H.; Wong, L. H.; Mhaisalkar, S. G. *J. Phys. Chem. C* **2011**, *114*, 1331−1336.
(16) Ginley, D. S.; Bright, C. *MRS Bull.* **2000**, *25*, 15−21.
(17) Minami, T. *Semicond. Sci. Technol.* **2005**, *20*, S35−S44.
(18) Chiang, H. Q.; Wager, J. F.; Hoffman, R. L.; Jeong, J.; Keszler, D. A. *Appl. Phys. Lett.* **2005**, *86*, 013503−1−013503−3.

(19) Gubbala, S.; Chakrapani, V.; Kumar, V.; Sunkara, M. K. *Adv. Funct. Mater.* **2008**, *18*, 2411−2418.
(20) Gubbala, S.; Russell, H. B.; Shah, H.; Deb, B.; Jasinski, J.; Rypkema, H.; Sunkara, M. K. *Energy Environ. Sci.* **2009**, *2*, 1302−1309.
(21) Cai, F.; Wang, J.; Yuan, Z.; Duan, Y. *Optoelectron. Lett.* **2011**, *7*, 321−324.
(22) Wang, C.; Du, G.; Ståhl, K.; Huang, H.; Zhong, Y.; Jiang, J. Z. *J. Phys. Chem. C* **2012**, *116*, 4000−4011.
(23) Xia, G.; Li, N.; Li, D.; Liu, R.; Xiao, N.; Tian, D. *Mater. Lett.* **2011**, *65*, 3377−3379.
(24) Spencer, M. J. S. *Prog. Mater. Sci.* **2012**, *57*, 437−486.
(25) Kim, I.-D.; Jeon, E.-K.; Choi, S.-H.; Choi, D.-K.; Tuller, H. *J. Electroceram.* **2010**, *25*, 159−167.
(26) Pan, J.; Shen, H.; Mathur, S. *J. Nanotechnol.* **2012**, *2012*, 917320.
(27) Shim, Y. S.; Moon, H. G.; Kim, D. H.; Jang, H. W.; Kang, C. Y.; Yoon, Y. S.; Yoon, S. J. *Sens. Actuators, B* **2011**, *160*, 357−363.
(28) Ramasamy, E.; Lee, J. *J. Phys. Chem. C* **2010**, *114*, 22032−22037.
(29) Barth, S.; Hernandez-Ramirez, F.; Holmes, J. D.; Romano-Rodriguez, A. *Prog. Mater. Sci.* **2010**, *55*, 563−627.
(30) Comini, E. *Anal. Chim. Acta* **2006**, *568*, 28−40.
(31) Dou, X.; Sabba, D.; Mathews, N.; Wong, L. H.; Lam, Y. M.; Mhaisalkar, S. *Chem. Mater.* **2011**, *23*, 3938−3945.
(32) Ramakrishna, S.; Jose, R.; Archana, P. S.; Nair, A. S.; Balamurugan, R.; Venugopal, J.; Teo, W. E. *J. Mater. Sci.* **2010**, *45*, 6283−6312.
(33) Reneker, D. H.; Yarin, A. L. *Polymer* **2008**, *49*, 2387−2425.
(34) Sigmund, W.; Yuh, J.; Park, H.; Maneeratana, V.; Pyrgiotakis, G.; Daga, A.; Taylor, J.; Nino, J. C. *J. Am. Ceram. Soc.* **2006**, *89*, 395−407.
(35) Kumar, E. N.; Jose, R.; Archana, P. S.; Vijila, C.; Yusoff, M. M.; Ramakrishna, S. *Energy Environ. Sci.* **2012**, *5*, 5401−5407.
(36) Dong, J.; Drabold, D. A. *Phys. Rev. B* **1996**, *54*, 10284−10287.
(37) Pan, Y.; Inam, F.; Zhang, M.; Drabold, D. A. *Phys. Rev. Lett.* **2008**, *100*, 206403.
(38) Ikhmayies, S. J.; Ahmad-Bitar, R. N. *Phys. Scr.* **2011**, *84* (5), 055801.
(39) Wijeratne, K.; Akilavasan, J.; Thelakkat, M.; Bandara, J. *Electrochim. Acta* **2012**, *72*, 192−198.
(40) Zaban, A.; Greenshtein, M.; Bisquert, J. *ChemPhysChem* **2003**, *4*, 859−864.
(41) Ferber, J.; Stangl, R.; Luther, J. *Sol. Energy Mater. Sol. Cells* **1998**, *53*, 29−54.
(42) Zaban, A.; Greenshtein, M.; Bisquert, J. *ChemPhysChem* **2003**, *4*, 859−864.
(43) Bisquert, J.; Zaban, A.; Greenshtein, M.; Mora-Sero, I. *J. Am. Chem. Soc.* **2004**, *126*, 13550−13559.
(44) Mukherjee, K.; Teng, T. H.; Jose, R.; Ramakrishna, S. *Appl. Phys. Lett.* **2009**, *95*, 012101−012103.
(45) Zhu, K.; Vinzant, T. B.; Neale, N. R.; Frank, A. J. *Nano Lett.* **2007**, *7*, 3739−3746.
(46) Bisquert, J.; Garcia-Belmonte, G.; Fabregat-Santiago, F.; Ferriols, N. S.; Bogdanoff, P.; Pereira, E. C. *J. Phys. Chem. B* **2000**, *104*, 2287−2298.
(47) Wang, Q.; Ito, S.; Grätzel, M.; Fabregat-Santiago, F.; Mora-Sero, I.; Bisquert, J.; Bessho, T.; Imai, H. *J. Phys. Chem. B* **2006**, *110*, 25210−25221.
(48) Bisquert, J.; Garcia-Belmonte, G.; Bueno, P.; Longo, E.; Bulhões, L. O. S. *J. Electroanal. Chem.* **1998**, *452*, 229−234.
(49) Bisquert, J.; Garcia-Belmonte, G.; Fabregat-Santiago, F.; Ferriols, N. S.; Bogdanoff, P.; Pereira, E. C. *J. Phys. Chem. B* **2000**, *104*, 2287−2298.
(50) Bisquert, J. *Phys. Chem. Chem. Phys.* **2003**, *5*, 5360−5364.
(51) Archana, P. S.; Jose, R.; Vijila, C.; Ramakrishna, S. *J. Phys. Chem. C* **2009**, *113*, 21538−21542.
(52) Archana, P. S.; Jose, R.; Mein Jin, T.; Vijila, C.; Yusoff, M. M.; Ramakrishna, S. *J. Am. Ceram. Soc.* **2010**, *93*, 4096−4102.
(53) Benkstein, K. D.; Kopidakis, N.; van de Lagemaat, J.; Frank, A. J. *J. Phys. Chem. B* **2003**, *107*, 7759−7767.
(54) Van de Lagemaat, J.; Frank, A. J. *J. Phys. Chem. B* **2001**, *105*, 11194−11205.

(55) Archana, P. S.; Jose, R.; Yusoff, M. M.; Ramakrishna, S. *Appl. Phys. Lett.* **2011**, *98*, 152106.

(56) Bisquert, J. *Phys. Chem. Chem. Phys.* **2000**, *2*, 4185−4192.

22120

dx.doi.org/10.1021/jp304876j | *J. Phys. Chem. C* 2012, 116, 22112−22120